Supporting Information

Tailoring an Iron-Based Metal-Organic Framework for Zn-ORR/CER Battery

Sukhjot Kaur,[a] Safa Gaber,[b] Kalpana Garg,[a] Abdul Khayum Mohammed,[b] Ankur Bordoloi,[c] Harpriya Minhas,[d] Biswarup Pathak,[d] Dinesh Shetty*[b, e] and Tharamani C. Nagaiah*[a]

[a]*Department of Chemistry, Indian Institute of Technology Ropar, Rupnagar, Punjab, 140001 India E-mail: tharamani@iitrpr.ac.in.*

[b]*Department of Chemistry, Khalifa University of Science & Technology, Abu Dhabi, P.O. Box 127788, United Arab Emirates E-mail: dinesh.shetty@ku.ac.ae.*

[c]*Nanocatalysis (LSP Division), CSIR-Indian Institute of Petroleum, Dehradun, Uttarakhand, 248005 India*

[d]*Department of Chemistry, Indian Institute of Technology Indore, Indore, Punjab, 140001 India.*

[e]*Center for Catalysis & Separations (CeCaS), Khalifa University of Science & Technology, Abu Dhabi, P.O. Box 127788, United Arab Emirates*

Experimental section

Chemicals required

Isopropyl alcohol (C_3H_7OH, Merck), hydrochloric acid (HCl, 35 %, Merck), sulfuric acid (H_2SO_4, 95-97 %, Loba Chemie), potassium hydroxide (KOH, 85 %, Loba Chemie), Zinc acetate ($Zn(OAc)_2$, 98 %, SpectroChem) are of analytical grade and were used as received. Deionized (DI) water was obtained from the Millipore system (> 12 Ω). triformylphloroglucinol (Tp) >95% was purchased from 'Hygeia laboratories'. Graphene nanoplatelet and $FeCl_3.6H_2O$ were purchased from 'Sigma Aldrich'.

Synthesis of Fe-Tp-x%(G)

Fe-Tp-X%(G) materials were synthesized using a mechanochemical mixing method followed by thermal treatment. The general procedure involved the precise blending of *1,3,5*-triformylphloroglucinol (Tp), iron(III) chloride hexahydrate ($FeCl_3.6H_2O$) in 1:1 molar ratio with varying weight percentages of graphene nanoplatelets (GNP) (5, 10, and 15 %wt.). For example, for the preparation of 10 wt.% graphene hybrid, 45.73 mg of graphene nanoplatelets were added to the mixture of 200 mg Tp and 257.25 mg of $FeCl_3.6H_2O$. After thorough mechanochemical mixing, the mixture was transferred to a sealed vial. The vial was then placed in an oven and subjected to thermal treatment at 90 °C for 24 hours. The as-prepared product was then subjected to several time washing with *N, N*, dimethylacetamide, water, THF and acetone. Finally, the purified hybrid material was dried in a vacuum oven overnight at 90 °C.

Synthesis of Fe-Tp

Fe-Tp was synthesized using a mechanochemical mixing method followed by thermal treatment. The procedure involved the precise blending of Tp, $FeCl_3.6H_2O$ in 1:1 molar ratio. After thorough mechanochemical mixing, the mixture was transferred to a sealed vial. The vial was then placed in an oven and subjected to thermal treatment at 90 °C for 24 hours. The as-prepared product was then subjected to several time washing with *N, N*, dimethylacetamide, water, THF and acetone. Finally, the purified hybrid material was dried in a vacuum oven overnight at 90 °C.

Physical characterization

The morphology of the prepared catalysts was analysed by field-emission scanning electron microscopy (FE-SEM, JSM 5800, JEOL) and the elemental composition using the energy-dispersive X-ray spectroscopy (EDS, Inca X-cat, Oxford Instruments). The electronic states of catalysts were depicted by X-ray photoelectron spectroscopy (XPS, Thermo Fisher Scientific's Escalab Xi instrument). Further, topographic images were obtained using high-resolution transmission electron microscopy (HR-TEM, FEI Themis, 300 kV). Fourier transform infrared (FT-IR) spectra were obtained using a BRUKER TENSOR-2 spectrometer equipped with a zinc selenide (ZnSe) window. The measurements were performed in the frequency range of 600–4000 cm^{-1} with a spectral resolution of 4 cm^{-1} and 100 scans. Porosity measurements were conducted on a Micromeritics 3-Flex gas sorption analyzer. Powder X-ray diffraction measurements were performed on Panalytical X'Pert PRO Powder Diffractometer with Cu Kα (λ = 1.5418 Å) radiation source operating at 40 kV and 40 mA. The samples were analyzed over the 2θ range of 10-50° with a step size of 0.02° (2θ).

Electrochemical in-situ Raman spectroscopy

Electrochemical in-situ Raman spectroscopy was performed on Horiba Scientific Raman instrument using 532 nm laser and integrated with Metrohm potentiostat/galvanostat (Autolab PGSTAT204). The laser was stabilised at 532 nm laser. The measurement was done using the home-made cell consisting of Fe-Tp-10% G coated on carbon paper as working electrode, graphite and Ag/AgCl/3 M KCl as counter and reference respectively and 0.4 M HCl as electrolyte and the laser was focused on the electrolyte.

Electrochemical investigation

Preparation of catalyst slurry

For the preparation of slurry, ~1.5 mg of the catalyst was grinded in mortar and pestle and was then added to 20 µL IPA and 480 µL of DI water followed by dispersion using ultrasonication for 30 mins. The prepared catalyst slurries were then drop casted on the graphite/carbon paper (5*5 cm^2) which was cleansed in 5 M HNO_3 to get rid of surface oxides, followed by ultrasonication for 15 minutes in water, and in isopropyl alcohol (IPA). The electrochemical measurements were performed using potentiostat/galvanostat Biologic VSP-300 connected with EC-Lab software. A three-electrode assembly, which comprised of Ag/AgCl/3M KCl as reference electrode and graphite electrode was employed as counter electrode was utilized for the half cell experiments. Initially, linear sweep voltammetry (LSV) experiments were recorded in the potential range of 1.0 to 2.0 V *vs.* RHE in 0.4 M HCl to measure the CER activity and from 1.0 to -0.2 V *vs.* RHE in O_2-saturated 0.4 M HCl for ORR activity. The hydrodynamic experiments *viz.*, rotating disk electrode (RDE/RRDE) using a glassy carbon electrode (Ø 5mm) and Pt ring (as working electrode 2) obtained from Pine instruments which was integrated with a speed controlling unit (AFMSRCE, Pine Research Instrument Inc., USA) along with a modular potentiostat/galvanostat (Autolab PGSTAT 302N).

Further, electrochemical impedance spectroscopy (EIS) measurements were performed at 1.7 V vs. RHE under illumination over a frequency range from 20 kHz to 20 mHz. Further, to obtain charge transfer resistance (R_{ct}) the EIS curves were fitted using Z-fit option in EC-Lab and an appropriate equivalent circuit. Also, electrochemical surface area (ECSA) was estimated by electrochemical double-layer capacitance (C_{dl}) *via* CV plots obtained at different scan rates ranging from 20-200 mV s^{-1}, with a potential sweep ranging from 0.80 to 0.87 V *vs.* RHE. The C_{dl} can be calculated from the slope (k) of the current density against scan rate at 0.83 V *vs.* RHE.

Further, the ECSA was estimated according to the equation:

$$ECSA = \frac{C_{dl}}{C_s}$$

where C_s is a specific capacitance of 40 µF cm^{-2}

All the potential are converted to the RHE scale for uniformity unless detailed otherwise.

$$E_{RHE} = E_{Ag/AgCl} + E^{\circ}_{Ag/AgCl} + 0.059\ pH$$

Where E_{RHE} is the converted potential *vs.* RHE, $E_{Ag/AgCl}$ is the experimentally measured potential *vs.* Ag/AgCl (saturated KCl), and $E^{\circ}_{Ag/AgCl}$ is 0.1976 V at 25 °C.

K-L plot analyses

The Koutecky-Levich (K-L plots) were extracted from RDE polarization curves using the formulae:

$$1/j = {}^{1}/_{j_k} + {}^{1}/_{j_d}$$

Where,

'j' stands for the measured current density

'j_k' and 'j_d' represent kinetic and diffusion current densities respectively.

Furthermore, the slope of the K-L plot was calculated by linearly fitting graph between inverse of current density (y-axis) and inverse of square root of rotation rate (x-axis) to find number of electrons transferred during oxygen reduction reaction and following equation was used:

$$j_d = 0.62nFD^{2/3}\upsilon^{-1/6}D_{O2}$$

Here,

n represents the number of electrons transferred during the ORR

F is Faraday constant (96500 C mol^{-1})

D is diffusion coefficient of dissolved oxygen ($1.43*10^{-5}$ cm^2 s^{-1})

υ is kinematic viscosity ($1.13*10^{-2}$ cm^2 s^{-1})

D_{O2} represents concentration of dissolved oxygen (1.61 mol cm^{-3}) in 0.4 M HCl.

The ring electrode was polarized at 1.1 V *vs.* RHE to detect the produced H_2O_2.

The % H_2O_2 and F.E. of H_2O_2 was calculated using the formulae as follows:

$$\%H_2O_2 = \frac{200\, x \frac{I_r}{N}}{I_d + \frac{I_r}{N}}$$

$$F.E.\,(\%) = \frac{100\, x \frac{I_r}{N}}{I_d}$$

Where I_d is the disc current, I_r is the ring current at particular potential and N is the collection efficiency of the electrode (0.36).

Electrochromic effect studies

Electrochromic effect was studied using *in-situ* spectro electrochemistry and the measurements were performed using Autolab spectrophotometer-UB (200-850 nm). The Autolab compact deuterium/halogen light source (200-2500 nm) was used as the light output with Avantes cell holder. The optical fibers had the dimensions of 2 m in length and 200 µm in diameter and were used to connect the electro-spectrophotometer and light source. Chronoamperometry at different potentials was performed for 5 mins each with simultaneous recording of UV spectra. The color change was noted and captured with change in the potential.

SECM studies[1-13]

SECM studies were used to provide localized electrocatalytic activity of Fe-Tp and Fe-Tp-10% G and were carried out using Sensolytics Base SECM (Sensolytics, Bochum, Germany) with four electrode

probe system having stepper-motor-driven x-y-z stages and an additional three-axis piezo-positioning system having a HighRes provision for stepper motor, working in conjunction with the bi-potentiostat (Autolab 204, Metrohm). The visualization of the local electrocatalytic activity of the catalysts towards ORR in 0.4 M HCl was done via redox competition mode of SECM (RC-SECM). It is done by polarising both the WE1 (Au microelectrode) and WE2 at ORR potentials; however, here a pulse potential profile was applied to the WE1. The cell setup consists of microelectrode (Ø 100 µm) tip as working electrode 1 and GC plate as working electrode 2 with Ag/AgCl/3M KCl as reference electrode and Pt wire as counter electrode. The microelectrode was cleaned with the polishing cloth with different grades of alumina and rinsed and sonicated in DI water. Before the measurement, the microelectrode behavior of the electrode was tested using 5 mM of potassium hexacyanoferrate (II) trihydrate solution in 0.1 M KCl to obtain a steady state CV measurement. Also, tip positioning was ensured by the approach curve measurements at the three spots of the chosen area and tilt correction was ensured. Afterwards, the array scan measurements in the x-y direction were carried out in RC-SECM mode where both the tip and the substrate compete for the ORR. For data evaluation after measurement, MIRA software was utilized.

Local pH studies *via* microelectrochemical approach[14]

Electrochemical measurements were performed in a bipotentiostatic mode using an Autolab PGSTAT204 modular potentiostat/galvanostat. A custom-built microelectrochemical cell was employed, featuring two working electrodes: a gold ultra-microelectrode (100 µm diameter) designated as WE1, and carbon paper drop-casted with Fe-Tp-10% G serving as WE2. A graphite electrode acted as the counter electrode, and an Ag/AgCl/3 M KCl electrode served as the reference electrode, all immersed in a 0.4 M HCl electrolyte. Prior to use, the microelectrode underwent cleaning with alumina slurry on a polishing cloth, followed by rinsing in water.

Full cell battery investigation

For battery studies, a two-electrode cell was built up in an H-type cell using polished Zn foil as anode with 1M KOH and 0.02 M $Zn(OAc)_2$ as anolyte and catalyst slurry drop coated on carbon paper (0.5 * 0.5 cm^2) as cathode in 0.4 M HCl as anolyte. Here, the catalyst loading on the carbon paper was 200 µg ml^{-1}. Both the catholyte and anolyte volume was 50 mL and the membrane area in contact with the electrolytes is of 1 cm diameter. The data was recorded using battery cycling system (BCS-810) run by BT-Lab V1.67 software. All the potentials were reported *vs.* Zn/Zn^{2+}. BPM employed for the stability studies of the battery was procured from Fumasep (FBM-PK) having a thickness of 130-160 µm with Na^+ and Cl^- as the counter ions for cation exchange and anion exchange layer, respectively.

Power Density and Energy Density calculations

$$Power\ density = \frac{VI}{A}$$

Power density is represented in mW cm^{-2}, V is the voltage in volts (V), *I* is the discharge current in mA, A represents the geometric area of the electrode and I/area gives the current density in mA cm^{-2}.

In this case, the discharge voltage (y-axis) and current density (x-axis) were multiplied and plotted as j *vs.* power density curve. The value at the maxima of the plateau was considered as the maximum power density obtained.

$$Energy\ density = \frac{VIt}{m}$$

Energy density is depicted in Wh kg^{-1}, V is the obtained voltage from the chronopotentiometry measurement at a current *I* (in mA), t is the time taken by the battery to completely discharge (in hours) and m is the mass of the zinc consumed during this discharge in kg.

In this case, voltage vs. time plot was obtained from the chronopotentiometry measurements and the x-axis of the plot (i.e. time in hours) was multiplied with the plateau voltage (V) obtained and current (mA) at which the measurement is performed, followed by dividing with the difference in the mass of Zn before and after the measurement.

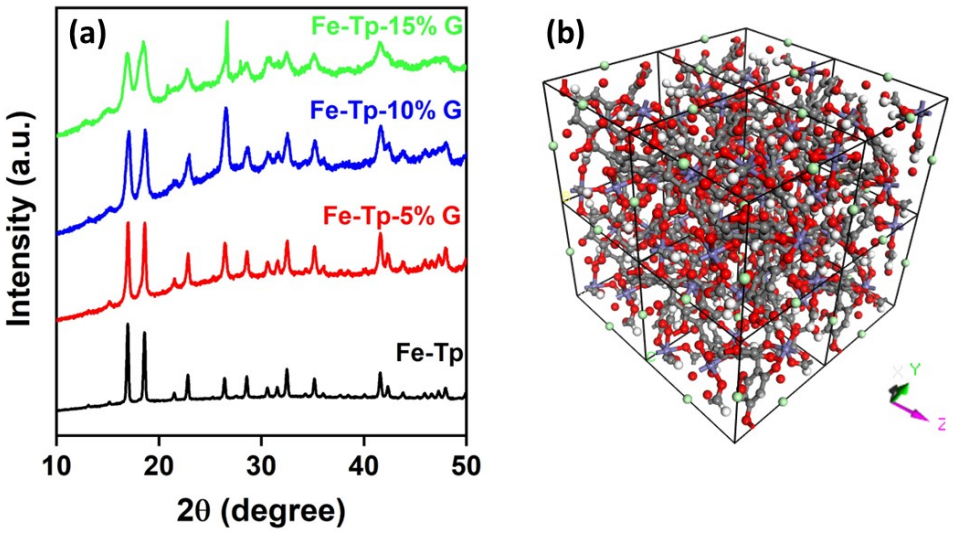

Figure S1. (a) P-XRD pattern of Fe-Tp and its variants with graphene (Fe-Tp-*x*% G) and (b) The theoretical model (2 x 2 x 2 unit cells) of Fe-Tp (carbon-gray; oxygen-red; chloride-green; hydrogen-white).

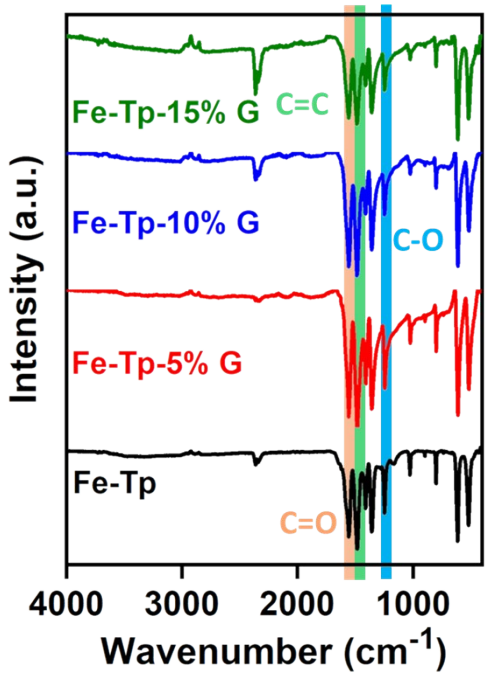

Figure S2: The FT-IR spectra of Fe-Tp-*x*% G with varying % of graphene.

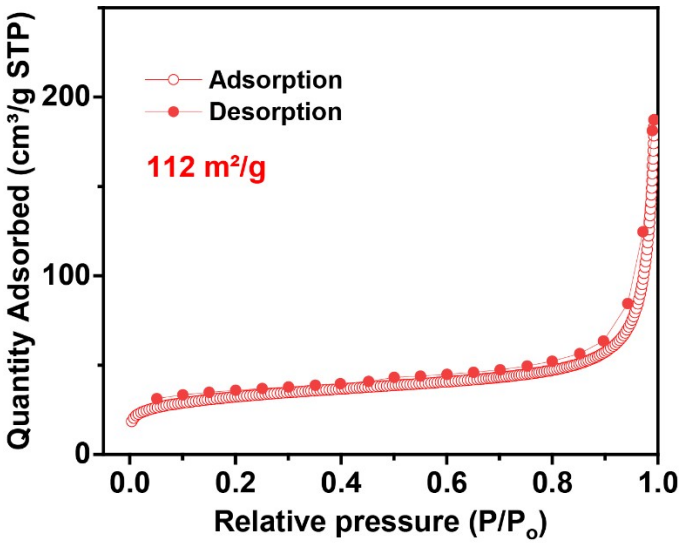

Figure S3. The N_2 gas adsorption analysis of Fe-Tp at 77 K.

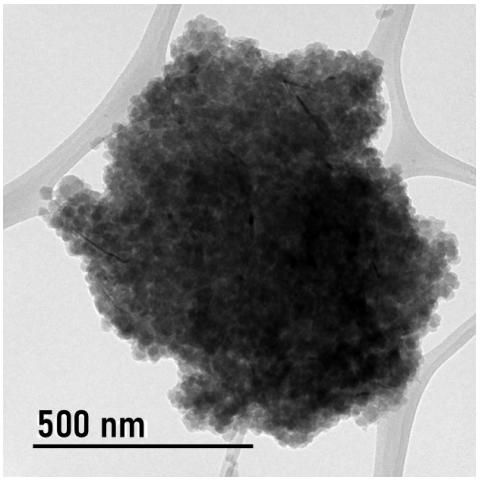

Figure S4. TEM image of Fe-Tp-10% G.

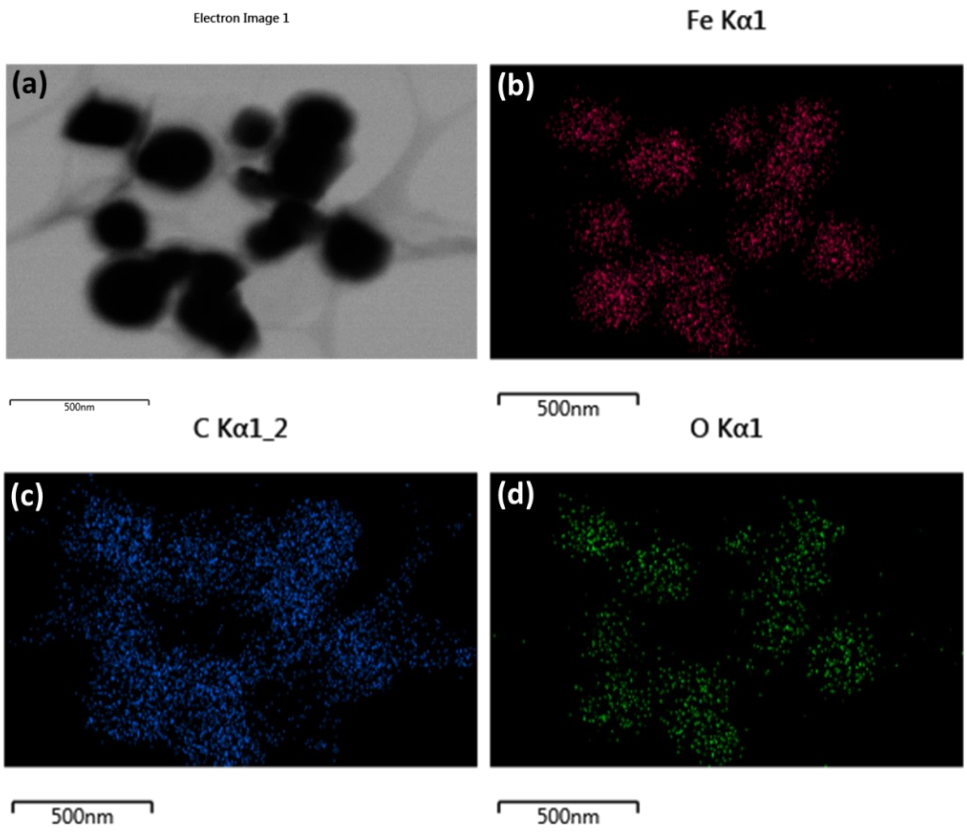

Figure S5. TEM-EDS dot mapping images for Fe-Tp.

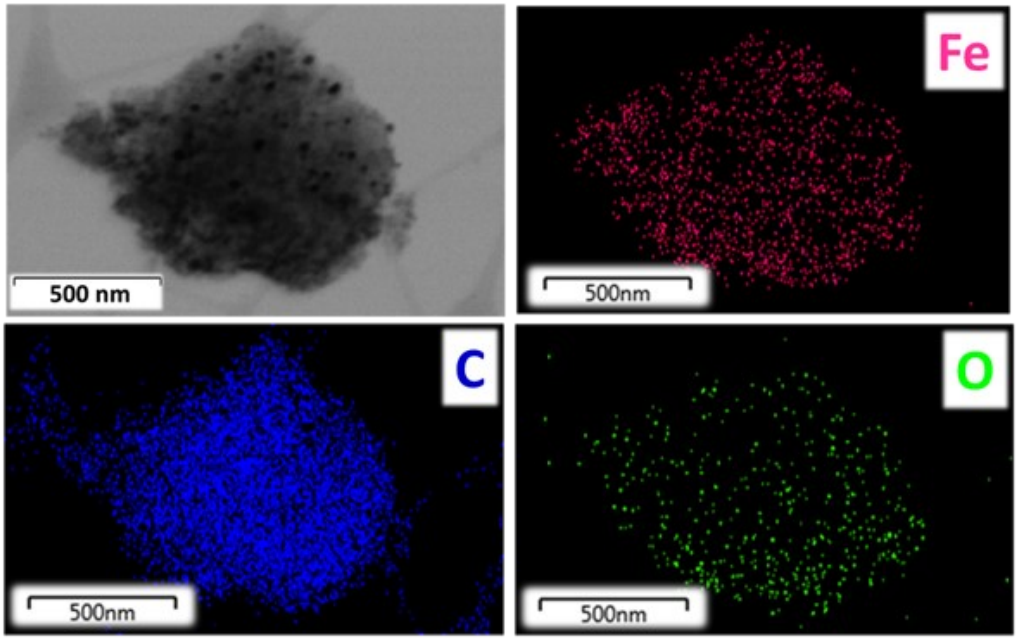

Figure S6. TEM-EDS dot mapping images for Fe-Tp-10% G.

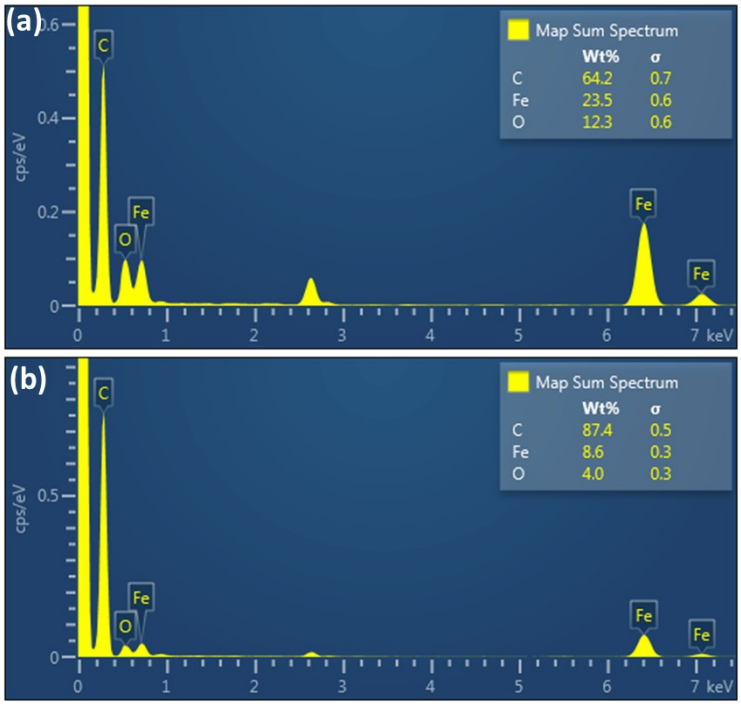

Figure S7. TEM-EDS spectra of (a) Fe-Tp and (b) Fe-Tp-10% G.

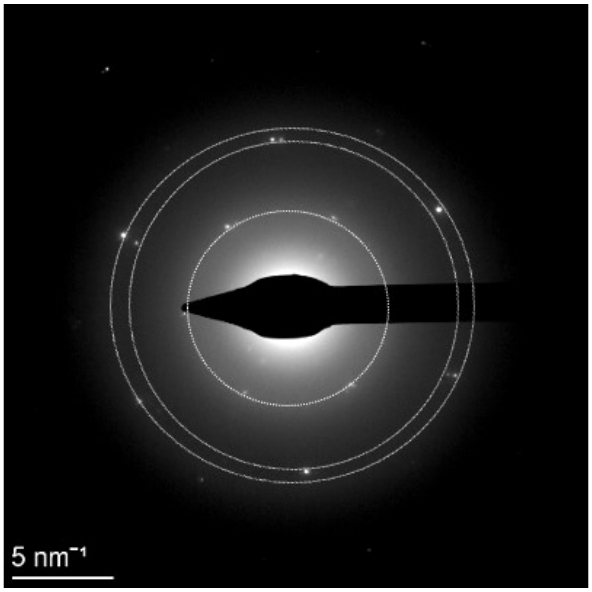

Figure S8. SAED pattern for Fe-Tp-10%G.

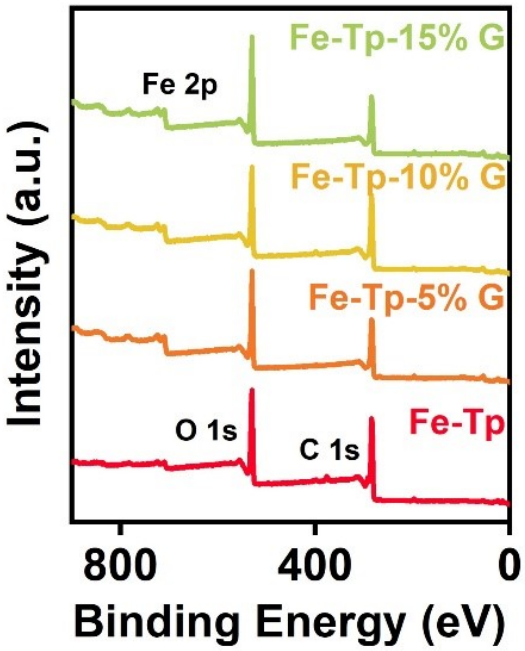

Figure S9. XPS survey spectra of Fe-Tp and variants of Fe-Tp-*x*% G.

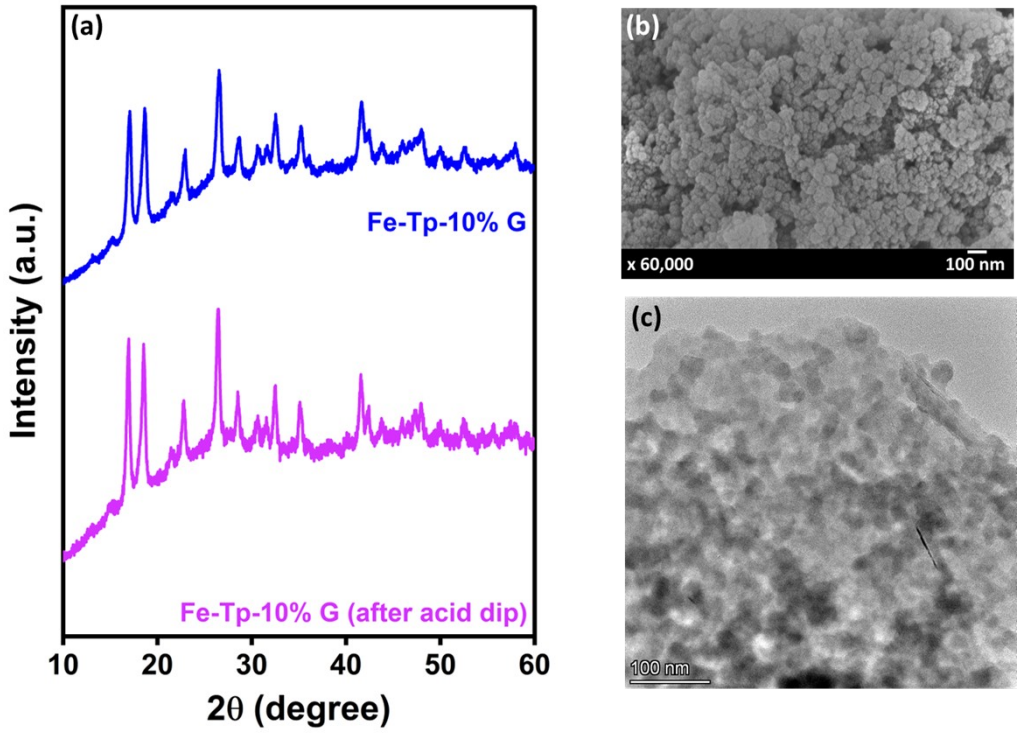

Figure S10. (a) P-XRD spectra, (b) FE-SEM and (c) HRTEM images of Fe-Tp-10% G after 24 h of dispersing in 0.4 HCl.

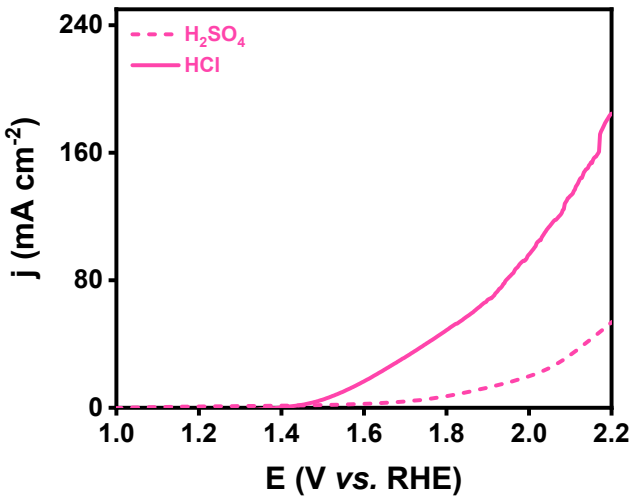

Figure S11. LSV curves for graphene in 0.2 M H_2SO_4 (for OER) and 0.4 M HCl (for CER).

Table S1. Comparison of CER and OER activity at different catalysts.

Catalyst	**E @ j= 100 mA cm^{-2}**	**j_{CER} @ E= 2V *vs.* RHE**	**j_{OER} @ E= 2V *vs.* RHE**
Graphene	2.01	~96.64	19.44
Fe-Tp	1.88	133.62	28.20
Fe-Tp-5% G	1.77	179.26	18.65
Fe-Tp-10% G	1.76	254.88	18.80
Fe-Tp-15% G	1.77	185.68	19.86

Table S2. Comparison table for CER activity with the reported literature in HCl media.

Catalysts	**Electrolyte**	**Overpotential @ 10 mA cm^{-2}**	**Zn-ORR/CER battery (Power density mW cm^{-2})**	**Ref.**
RuO_2(110)/Ru(0001)	0.5 M HCl	80	-	[15]
OCNT-PVIM-ZnPOM	0.4 M HCl	40	-	[5]
Co-NSC	0.4 M HCl	42	-	[7]
Cu-Fe_2O_3(5%)/ NC	0.4 M HCl	40	-	[16]
Tta-Dfp	0.4 M HCl	140	-	[13]
Ag-GD (Galvanic displacement)	0.4 M HCl	40	~4.4	[11]
Fe-Tp-10% G	**0.4 M HCl**	**100**	**5.4**	**This work**

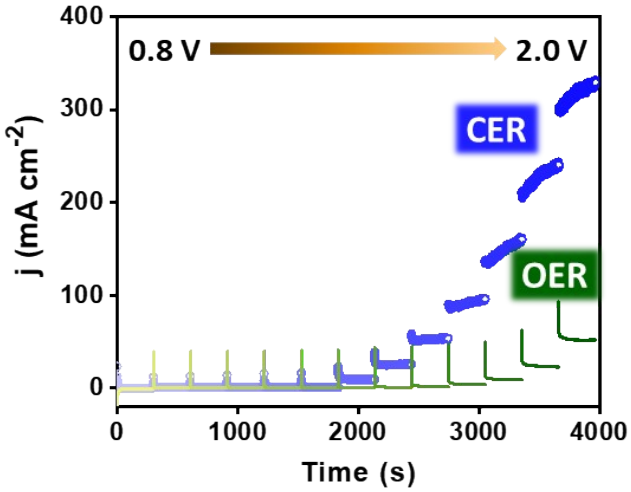

Figure S12. Sequential chronoamperometry measurements for Fe-Tp-10% G in 0.4 M HCl and 0.2 H_2SO_4.

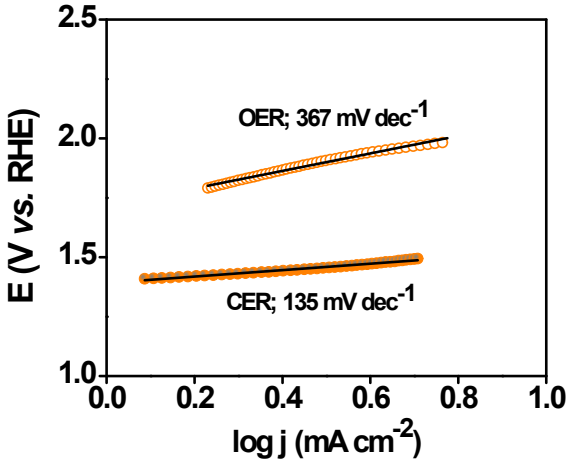

Figure S13. Tafel slopes for Fe-Tp-10% G extracted from Figure 2a.

Quantification of Chlorine gas using iodometry titration

In the course of chronoamperometric experiments, 200 mg of KI was added immediately into the electrolyte in order to trap the generated Cl_2. Following the chronoamperometry, the solution was kept to attain equilibrium. The resulting quantity was determined by performing Iodometric titration *vs.* 0.1 M $Na_2S_2O_3$ using 0.25 ml starch as end point indicator and the following reactions will take place.

$Cl_2 + KI \rightarrow I_3^- + Cl^-$ (Equation 1)

$I_3^- + 2\ S_2O_3^{2-} \rightarrow 3I^- + S_4O_6^{2-}$ (Equation 2)

Calculation

Total volume of 0.1 M $Na_2S_2O_3$ consumed during titration = *x* mL

Volume taken in the flask (0.4 M HCl and excess KI) = 80 mL

On applying the molarity equation:

$$M_1 * V_1 = M_2 * V_2$$

$$0.1\,M * x\,mL = M_2 * 80\,mL$$

$$M_2 = y\,M\,(I_3^-)$$

As can be seen in the stoichiometric equation two thiosulfate molecules are required for one (I_3^-), therefore the concentration of I_3^- or Cl_2 (C_{exp}) would be equal to = *y/2* M or mol/L.

Further, the amount of evolved chlorine was used to calculate the Faradaic efficiency as:

$$C_{theo} = \frac{i * t}{nF}$$

$$C_{theo} = \frac{z\,C}{2 * 96485\,C/mol} = Z'\,mol$$

Upon converting the obtained value in mol/l considering the 80 ml of volume taken to evolve the chlorine, F.E. is calculated as:

$$F.E.\,(\%) = \frac{C_{exp}}{C_{theo}} x\,100$$

Table S3. F.E. of chlorine obtained *via* iodometric titration method for graphene, Fe-Tp and Fe-Tp-10% G as catalysts.

Catalyst	**Vol. of $Na_2S_2O_3$ used (mL)**	**Conc. of I_3^- (y)**	**C_{exp} (y/2) (mol/L)**	**Charge (Q, Coulombs)**	**C_{theo} (mol/L)**	**FE (%)**
Graphene	0.08	0.0001	0.00005	0.99	0.000064	78
Fe-Tp	0.11	0.0001375	0.00006875	1.22	0.000079	87.03
Fe-Tp-10% G	0.11	0.0001375	0.00006875	1.10	0.00007125	96.49

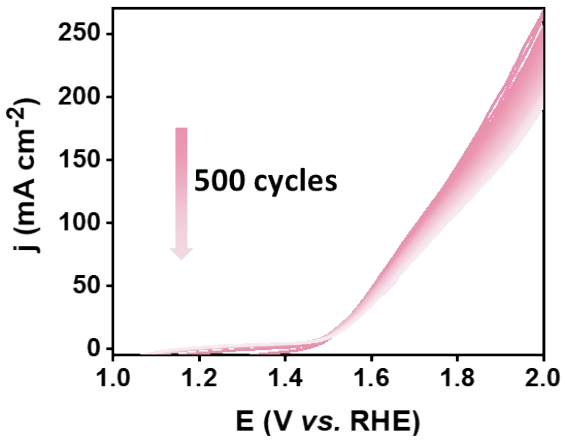

Figure S14. 500 LSV cycles for CER using Fe-Tp-10% G in 0.4 M HCl at a scan rate of 25 mV s^{-1}.

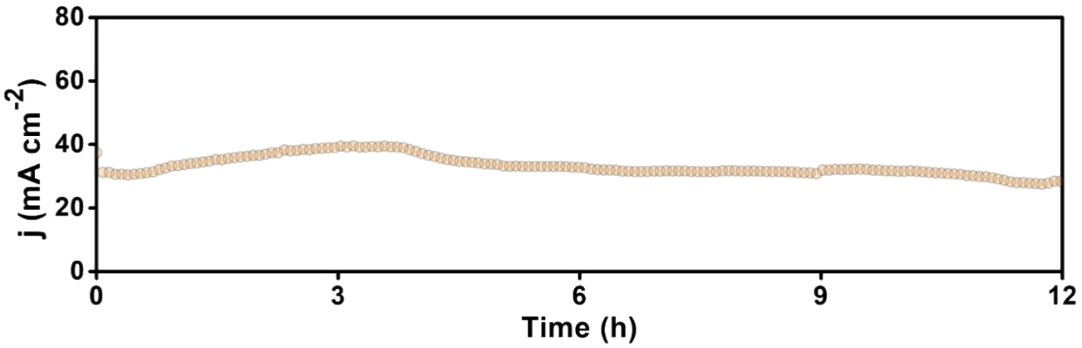

Figure S15. Chronoamperometry curve of Fe-Tp-10% G at 1.5 V for 12 h in 0.4 HCl.

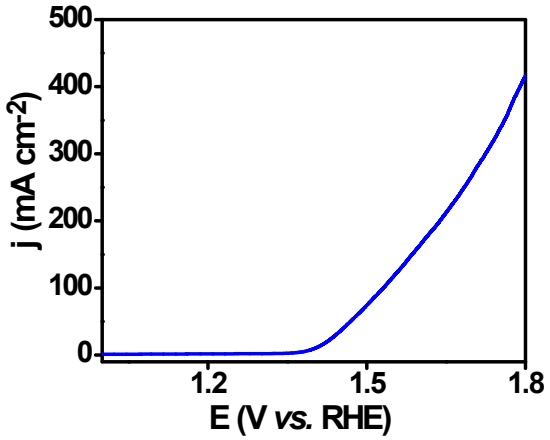

Figure S16. LSV curves for Fe-Tp-10% G in 5 M HCl at a scan rate of 5 mV s^{-1}.

MPAES analysis for metal leaching in the electrolyte:

MPAES analysis was done using Agilent Technologies instrument MY16360003 wherein firstly the Fe^{3+} calibration was formed with 0, 2, 5, 10, 20 and 50 ppm. The pump speed was 10 rpm and sample uptake time was 15 s. Fe was analysed at a wavelength of 248.327 nm.

Calibration Curves:

Fe (248.327 nm)
Intensity = (4685.05 * Concentration - 0.00) / (1 + 0.00 * Concentration)
Correlation coefficient: 1.00000

Standards	Intensity	Method Concentration	Calculated Concentration	% Error
Blank	0.00	0.00	0.00	N/A
2ppm	9425.82	2.00	2.01	0.50
5ppm	23250.41	5.00	4.98	0.40
10ppm	46277.18	10.00	9.93	0.70
20ppm	92771.91	20.00	20.01	0.05
50ppm	228394.44	50.00	50.03	0.06

Figure S17. Calibration data for known conc. of Fe using MPAES technique. (extracted from the instrument)

Table S4. Conc. of Fe^{3+} in the electrolyte using MPAES.

Electrolyte sample	Fe conc. (ppm) from MPAES
Before the test	-0.01
After 1h of CER	0.15
After 24h of CER	3.17

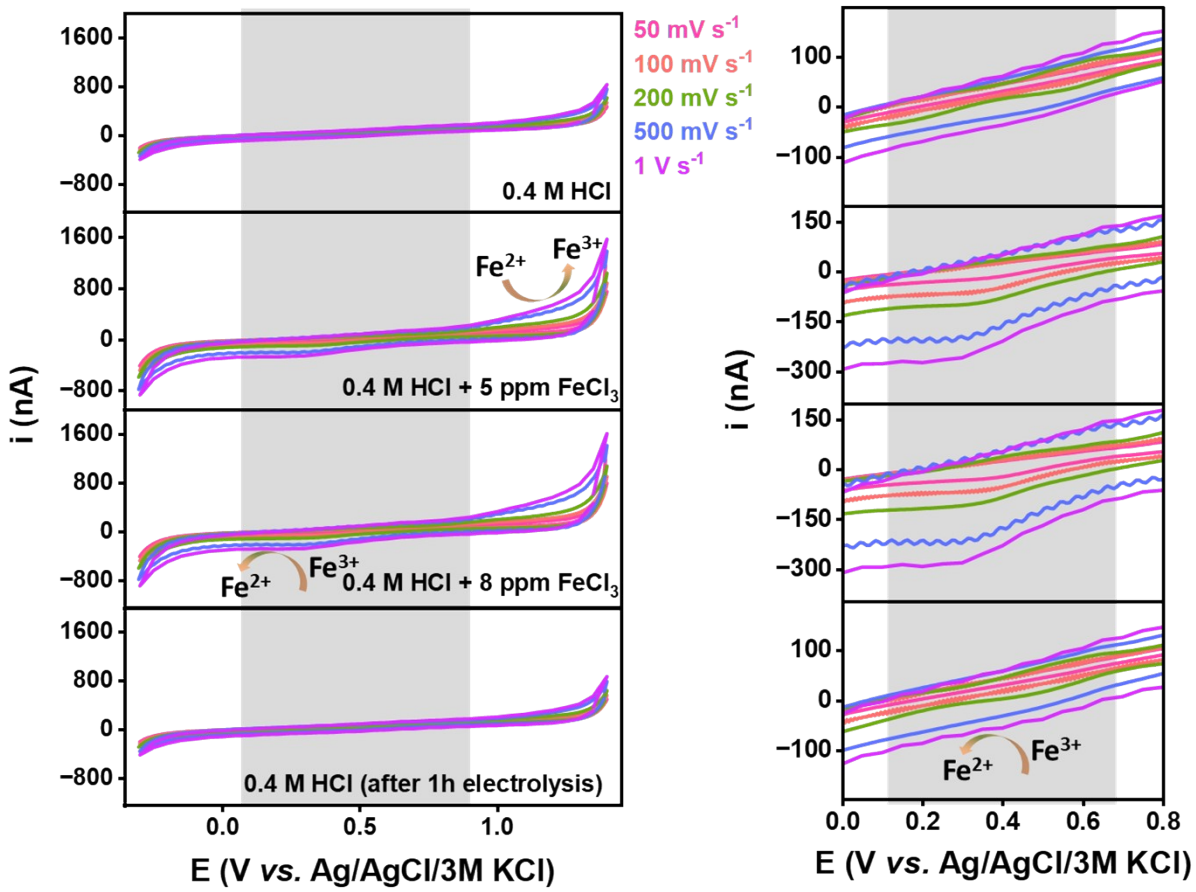

Figure S18. CV curves showing the presence/absence of Fe redox peaks observed in the electrolyte solution, with the zoomed Fe^{3+}/Fe^{2+} peak (right)

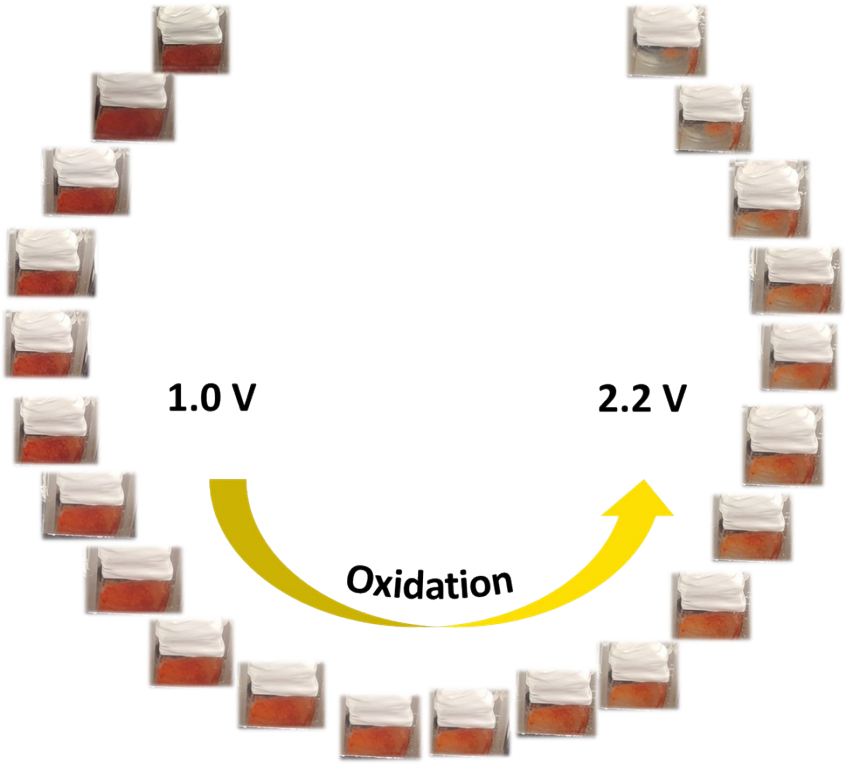

Figure S19. Photographs showing the electrochromic effect on Fe-Tp as an effect of applied oxidation potentials.

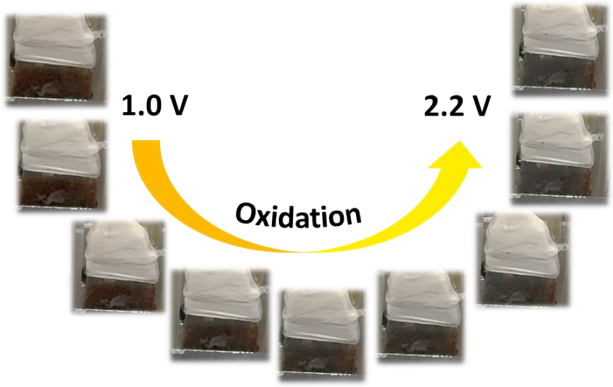

Figure S20. Photographs showing the electrochromic effect on Fe-Tp-10% G as an effect of applied oxidation potentials.

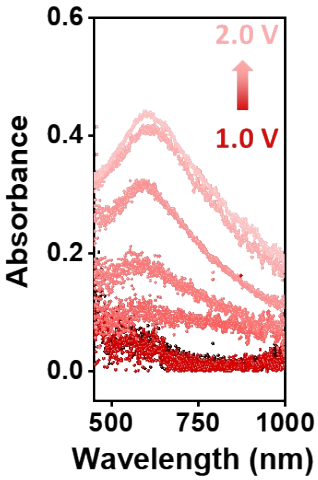

Figure S21. *In-situ* UV-Vis spectra recorded during CER at different potentials.

Figure S22. Photographs showing the reverse color change on Fe-Tp as an effect of applied reduction potential (-1.0 V)

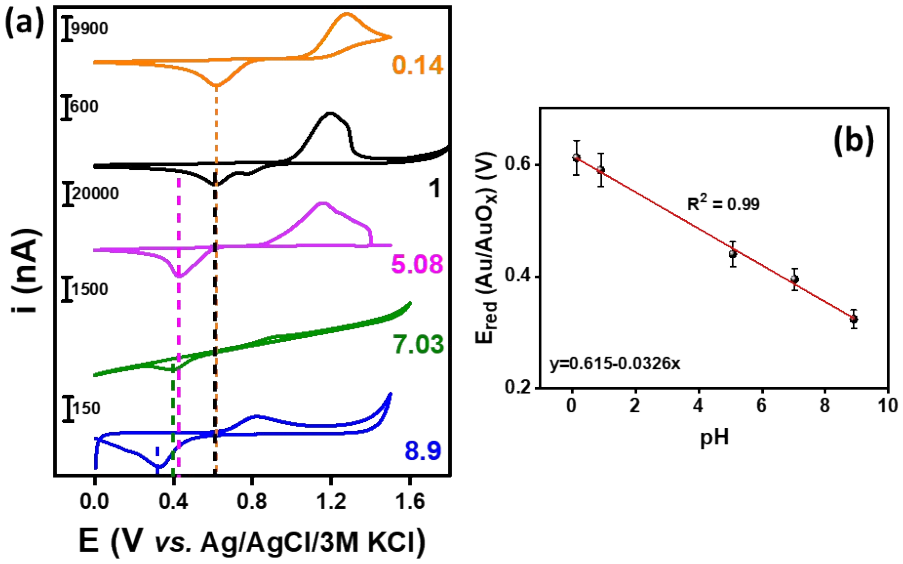

Figure S23. (a) CV curves of Au microelectrode in different pH solutions and (b) corresponding calibration (E_{red} *vs.* pH).

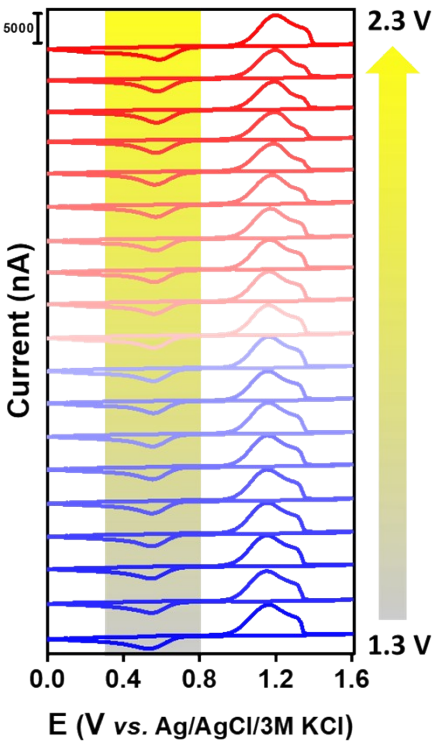

Figure S24. CV curves recorded on Au microelectrode (WE1) when substrate (WE2) was subjected to CER (ranging from 1.3 V to 2.3 V).

Computational details

The first principles spin polarized calculations were performed using the Vienna ab initio simulation package (VASP). The Generalized Gradient approximation with Perdew-Burke-Ernzerhof (GGA-PBE)[17] was employed to describe the exchange-correlations functionals, and the Projector Augmented Wave (PAW)[18] was utilized to describe the ion core and valence electron interactions. The cutoff energy for the plane-wave basis sets was set to 550 eV, and a conjugate gradient algorithm with an energy convergence criterion of 10-4 and Hellman-Feynman force convergence criteria of < 0.02 eVÅ-1 was utilized during structural optimizations.[19] Gaussian smearing of 0.2 eV and the DFT-D3 method were used to correctly define the van der Waals interactions.[20] To improve the description of the electronic correlation provided by conventional DFT in systems involving transition metals with localized d-electrons, a Hubbard-corrected DFT+U framework has been adopted with an optimal U=4.0 eV.[21] The Gibbs free energies of elementary steps during the CER were calculated using the computational hydrogen electrode (CHE) model proposed by Nørskov and co-workers by using the following equation[22]:

$$\Delta G = \Delta E + \Delta E_{ZPE} - T\Delta S - eU$$

Where ΔE is the hydrogen binding energy, ΔE_{ZPE} is the change in zero-point energy, T is the temperature (300 K), and ΔS is the entropy change for the reaction, U is the electrode potential referenced to the standard hydrogen electrode, and e is the transferred electronic charge. The ΔE_{ZPE} and entropies were calculated from harmonic oscillator approximation.[23] The zero-point energy (E_{ZPE}) was calculated using the following equation:

$$ZPE = \sum_i \frac{1}{2} h\nu_i$$

$$S_v = R \sum \frac{\hbar\nu_i}{k_B T\left(exp\left(\frac{\hbar\nu_i}{kT} - 1\right)\right)} - ln\left(1 - exp\left(\frac{\hbar\nu_i}{kT}\right)\right)$$

where h is the Planck constant, S_v is the vibrational entropy, R is the gas constant, k_B is the Boltzmann constant, ν_i is the frequency of the i_{th}vibrational mode and $\hbar = h/2\pi$. The adsorption energies of intermediates were calculated using the following equation:

$$E_{ads} = E(surface - (X)) - E(surface) - E(X)$$

where $E(surface - (X))$ is the optimized electronic energy of intermediate-adsorbed geometry on $graphene$, Fe-Tp MOF and Fe-Tp-G, $E(surface)$ is the optimized energy of the $graphene$, Fe-Tp MOF and Fe-Tp-G, and $E(X)$ is the optimized energy of the CER intermediates in the gas-phase, respectively.

The single molecular unit cells of Fe-Tp MOF and Fe-Tp @graphene, were optimized in 16.00 × 16.00 × 16.00 Å3 and 22.21 × 22.21 × 20.80 Å3 respectively, to minimize the interactions between periodic images. The Γ-centered (1×1×1) k-point grids were considered for the sampling of the Brillouin zone for the following calculations.

Free-energy changes for the CER mechanism were computed assuming the Volmer–Heyrovský mechanism.[23-25] In this context, we consider two different Volmer–Heyrovský pathways by referring to the formation of either a *Cl or an *OCl intermediate.[26]

(I) Pathway mediated by the *Cl intermediate:

ΔG1: * + Cl− (aq) ⇌ *Cl + e−

ΔG2: *Cl + Cl− (aq) ⇌ * + Cl2 (g) + e−

(II) Pathway mediated by the *OCl intermediate:

$$\Delta G3: *O + Cl^- (aq) \rightleftharpoons *OCl + e^-$$

$$\Delta G4: *OCl + Cl^- (aq) \rightleftharpoons *O + Cl2 (g) + e^-$$

In the above equation, *Cl, *O, and *OCl are the total free energies of the adsorbed intermediates, while (*) is the total energy of graphene, Fe-Tp MOF and Fe-Tp @ graphene without adsorbed intermediates.

Table S5: The most stable adsorption site and its corresponding adsorption energy values (Eads) in eV units for CER intermediates on graphene, Fe-Tp MOF and Fe-Tp-G.

Reaction Pathway	Graphene	Fe-Tp MOF	Fe-Tp-G
***Cl**	-0.51	-0.12	-0.36
***OCl**	-1.07	-0.86	-1.42

Table S6: Free-energy change (eV) of elementary steps step for graphene, Fe-Tp MOF and Fe-Tp-G for CER in an acidic medium at 1.36 V equilibrium potential.

Reaction Pathway	Steps	Graphene	Fe-Tp MOF	Fe-Tp-G
***Cl**	ΔG_1	-0.53	-1.11	-0.47
***OCl**	ΔG_3	-2.22	-2.02	-2.58

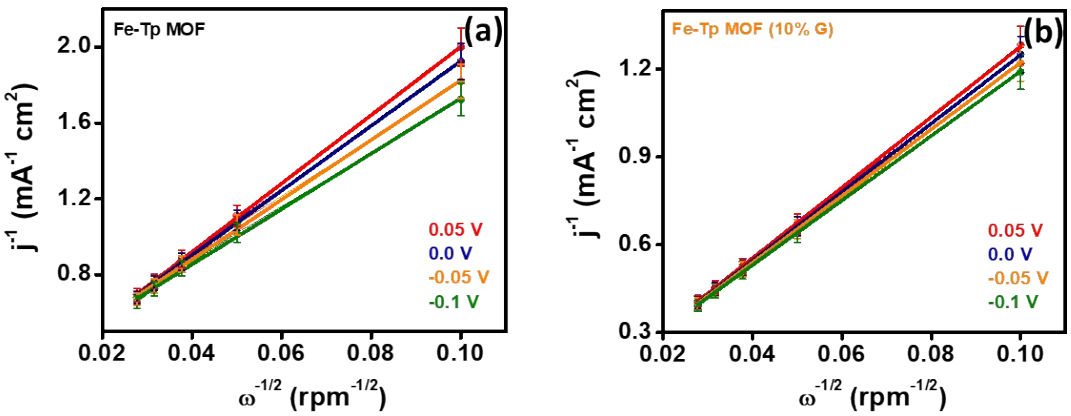

Figure S25. K-L plot for (a) Fe-Tp, (b) Fe-Tp-10% G at various potentials.

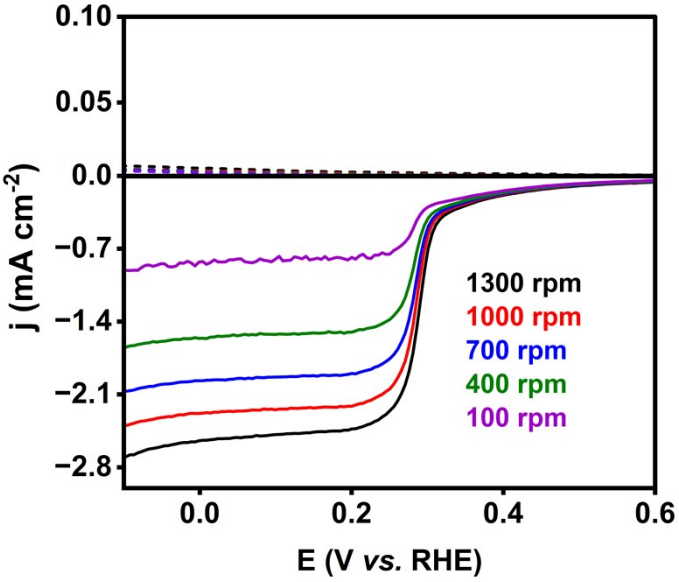

Figure S26. RRDE polarisation curves of Fe-Tp-10% G in O_2-saturated 0.4 M HCl at different rotation rates.

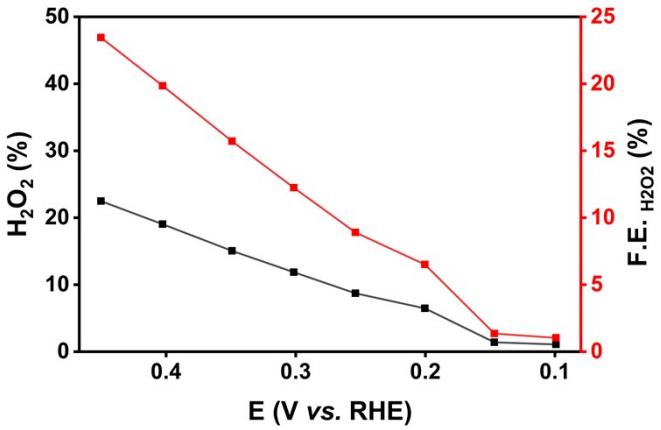

Figure S27. Percentage of H_2O_2, its F.E. and no. of electron transfer using Fe-Tp-10% G derived from RRDE curves (Figure S29) at different potentials.

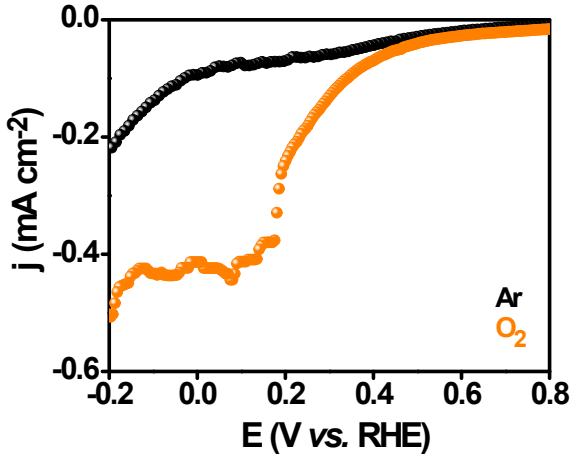

Figure S28. LSV curves for Fe-Tp-10% G in Ar and O_2 saturated 0.4 M HCl electrolyte under static conditions.

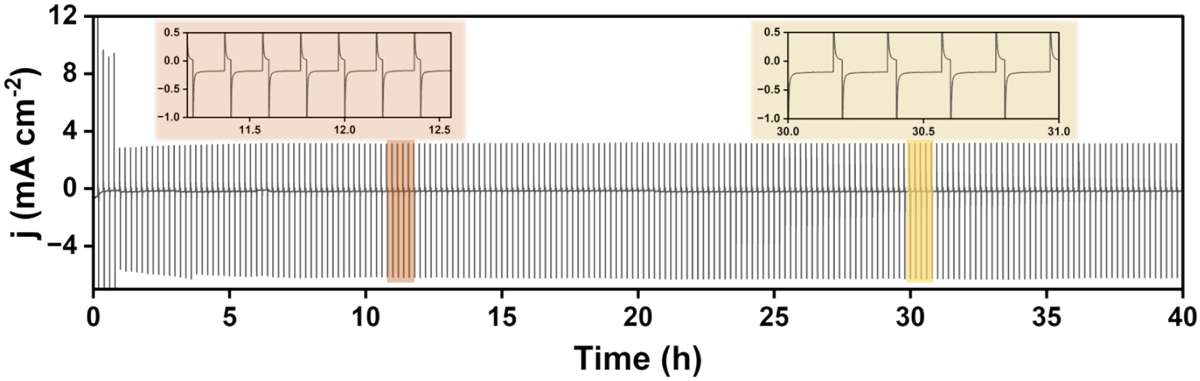

Figure S29. Chronoamperometric analysis performed for 10 minutes of operation at 0.0 V and 2 minutes of shutdown (i.e. system off) for Fe-Tp-10% G.

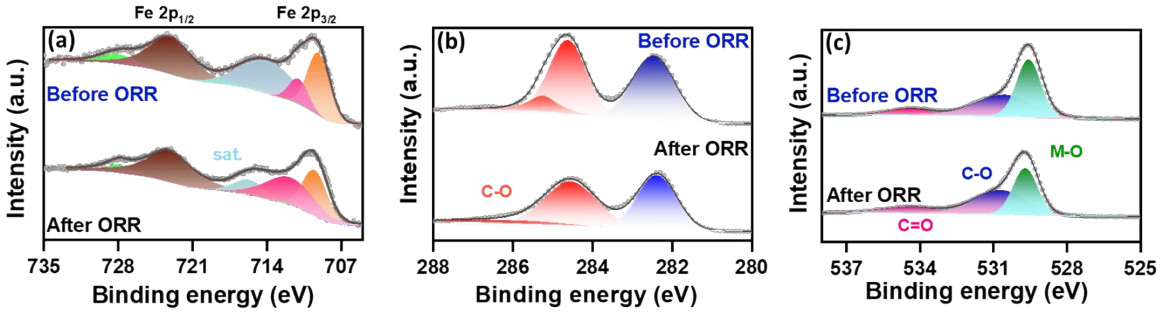

Figure S30. Comparison of XP spectra for (a) Fe2p, (b) C1s and (c) O1s before the experiment and after ORR.

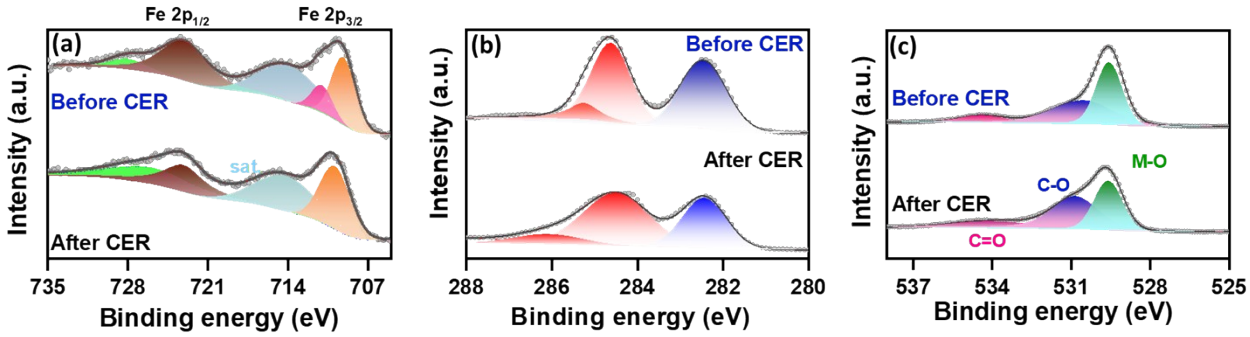

Figure S31. Comparison of XP spectra for (a) Fe2p, (b) C1s and (c) O1s before and after CER.

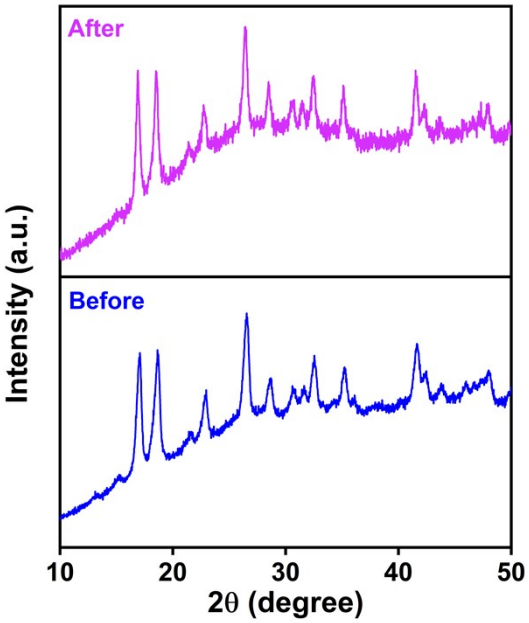

Figure S32. P-XRD pattern for Fe-Tp-10% G before and after CER.

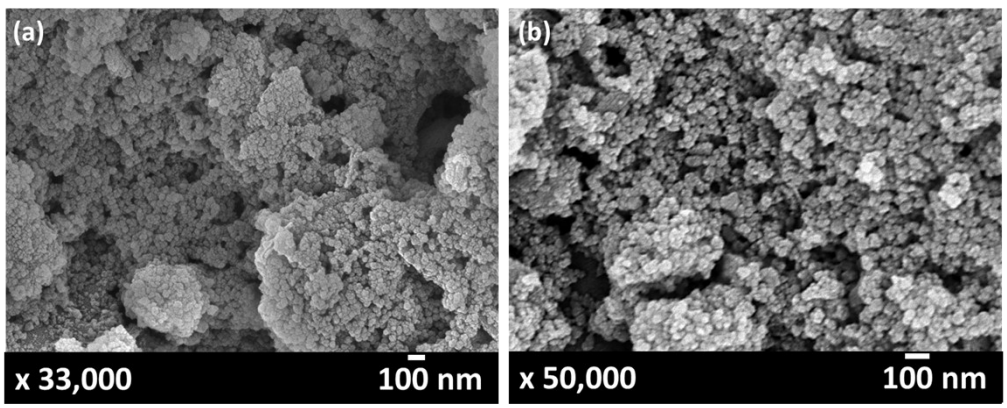

Figure S33. FE-SEM images for Fe-Tp-10%G (a) after CER and (b) after ORR.

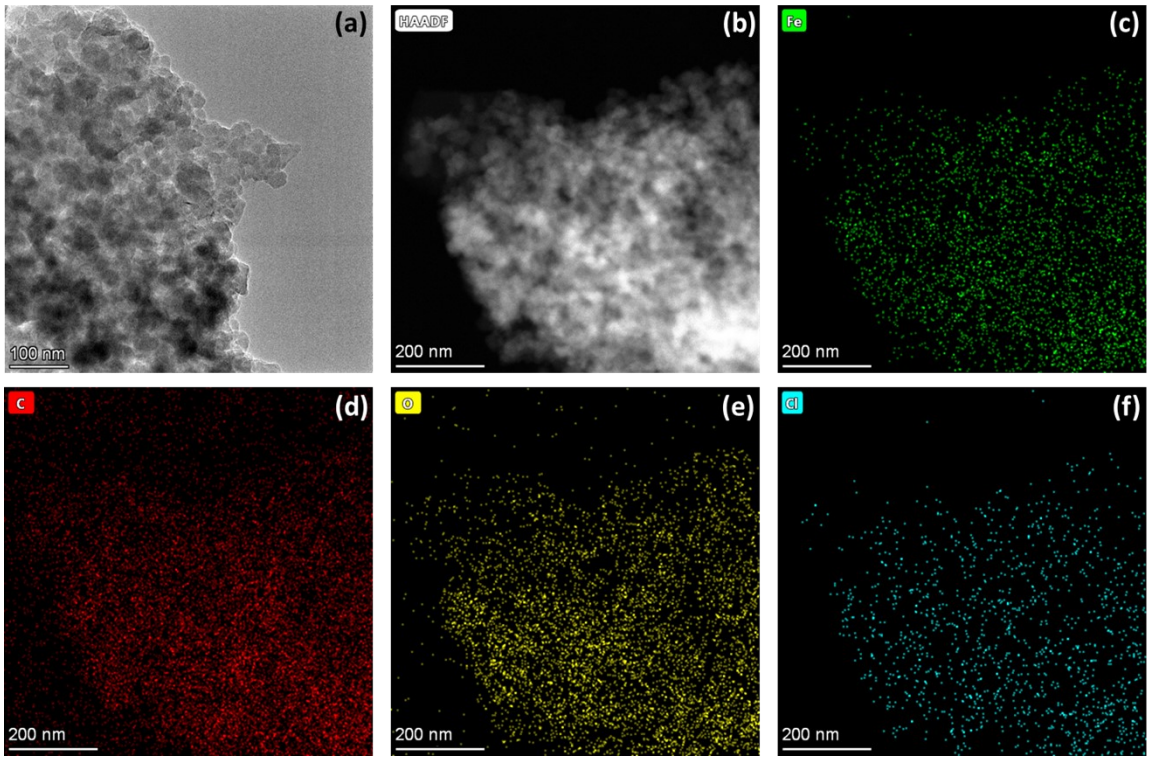

Figure S34. (a) TEM image of Fe-Tp-10% G after CER, (b) HAADF-STEM image and corresponding elemental dot mapping images for (c) Fe, (d) C, (e) O and (f) Cl.

Table S7. TEM-EDS spectral data for Fe-Tp-10% G after CER.

Z	Element	Family	Mass Fraction (%)	Mass Error (%)
6	C	K	75.57	2.48
8	O	K	14.82	3.02
26	Fe	K	9.60	1.32

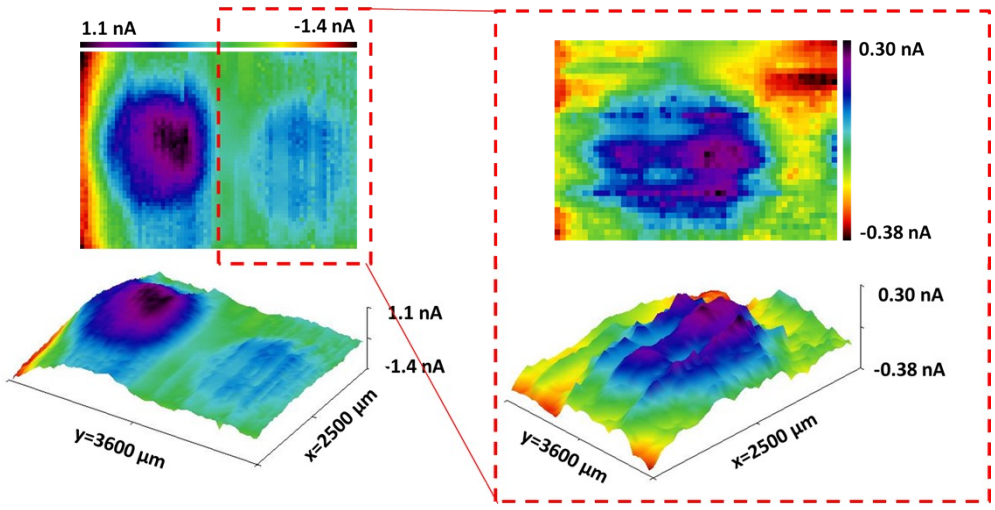

Figure S35. 2D and 3D SECM images of Fe-Tp and Fe-Tp-10% G when WE2 was polarised at 0.1 V.

The Nyquists plot from EIS studies (Figure S36) shows lower charge-transfer resistance (R_{ct}) for Fe-Tp-10% G (41.97 Ω) compared to Fe-Tp (95.29 Ω), which depict the faster kinetics the could be due to the presence of graphene. This was confirmed by higher double-layer capacitance (C_{dl}, 0.56 µF) and ECSA (1.4 mm^2, Figure S37) of Fe-Tp-10% G as compared to Fe-Tp (0.413 µF and 1.03 mm^2) by performing the cyclic voltammetry (CV) in the non-faradaic regions at different scan rates.

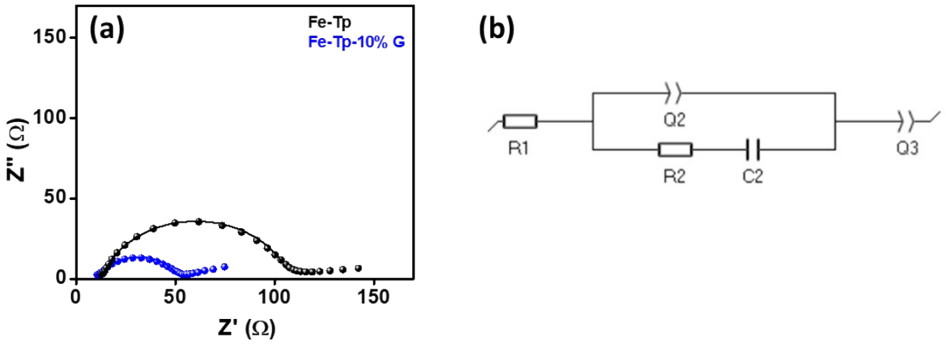

Figure S36. (a) Nyquist plot for Fe-Tp and Fe-Tp-10% G, (b) corresponding equivalent circuit obtained after fitting Nyquist plots

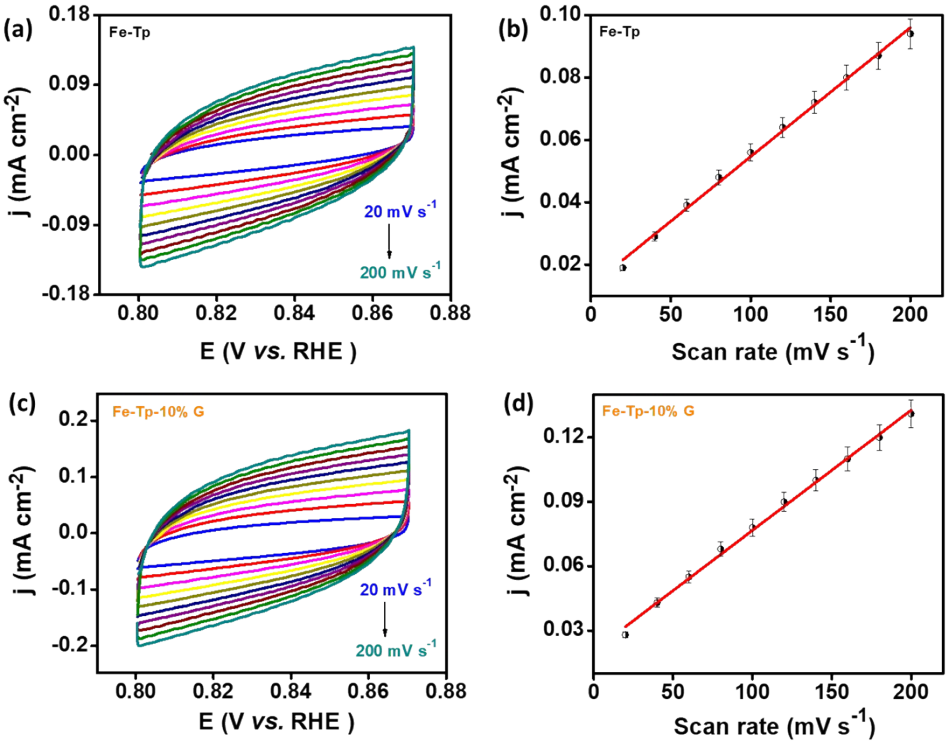

Figure S37. Cyclic voltammograms for (a) Fe-Tp, (c) Fe-Tp-10% G in non-faradaic region at different scan rates ranging from 20 mV s^{-1} to 200 mV s^{-1} and (b), (d) their corresponding current density *vs.* scan rate curves for measurement of C_{dl} and ECSA.

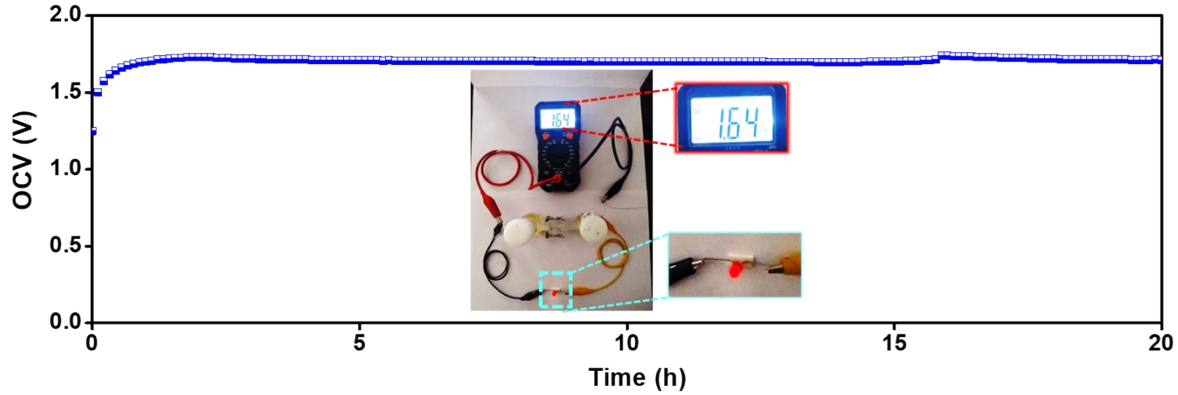

Figure S38. OCV measurement for assembled Zn-ORR/CER battery for 20 h using Fe-Tp-10% G.

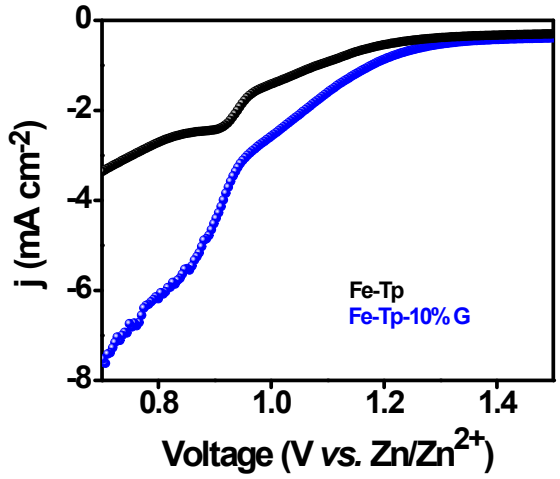

Figure S39. Discharge polarization curves for Fe-Tp, Fe-Tp-10% G in Zn-ORR/CER battery.

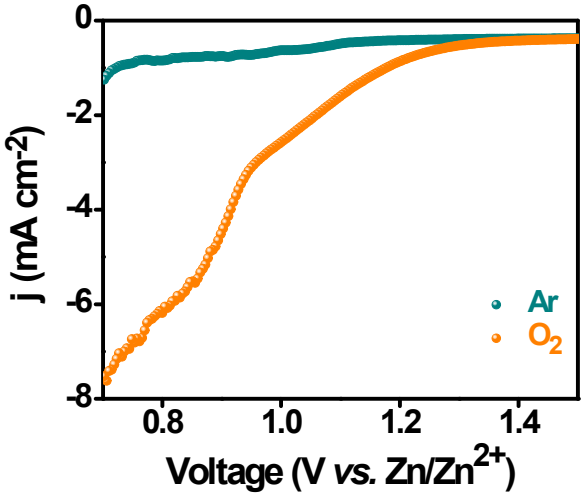

Figure S40. Discharge curves of the battery in Ar and O_2-saturated 0.4 M HCl for Fe-Tp-10% G.

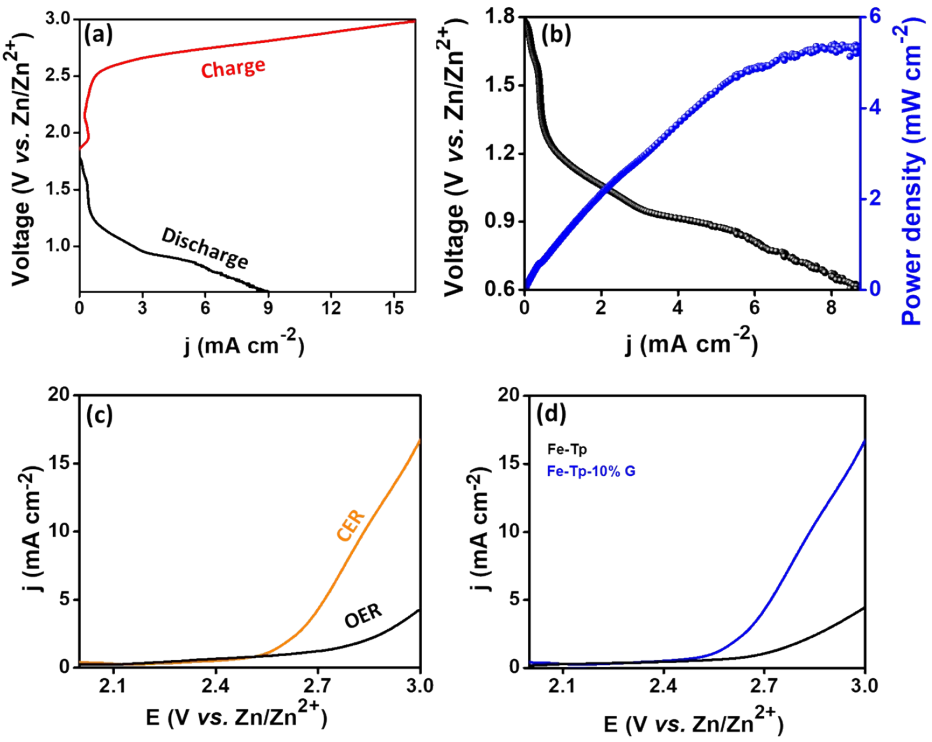

Figure S41. (a) Discharge and charge polarization curves for Zn-ORR/CER battery at 5 mV s^{-1}, (b) power density curve for Fe-Tp-10% G, (c) charge polarisation curves for Fe-Tp-10% G in 0.4 M HCl (CER) and 0.2 M H_2SO_4 (OER) and (d) charge polarization curves for Fe-Tp, and Fe-Tp-10% G in 0.4 M HCl.

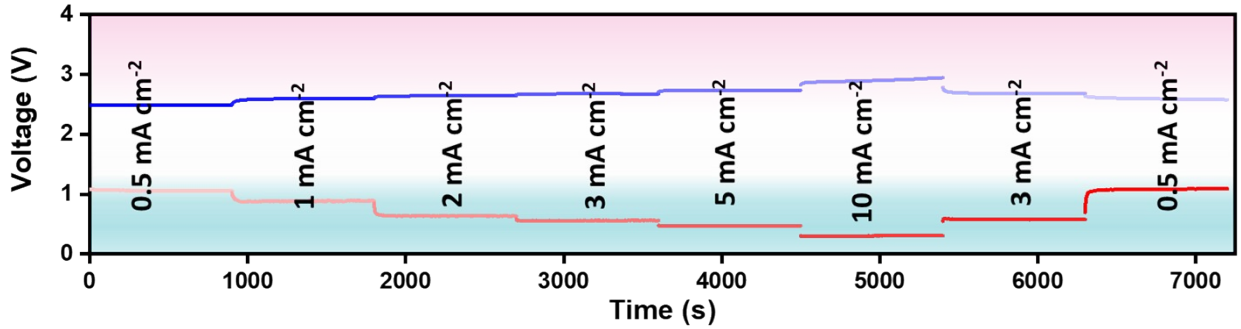

Figure S42. Chronopotentiograms for charging and discharging at different current densities for 15 mins each.

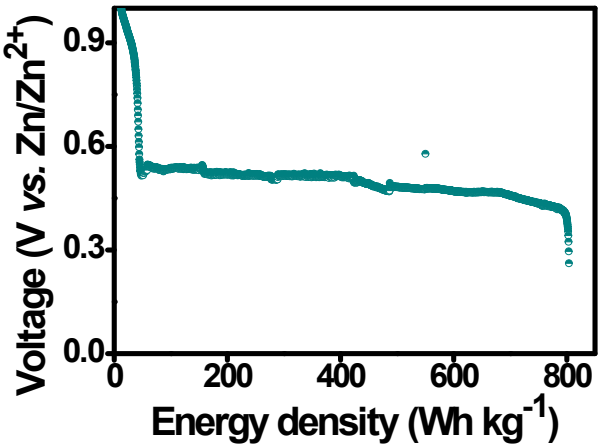

Figure S43. Energy density curve for the assembled Zn-ORR/CER battery using Fe-Tp-10% G.

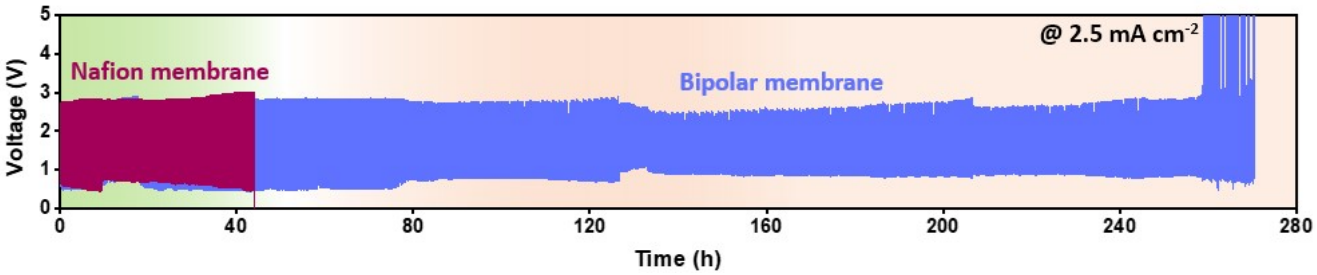

Figure S44. Galvanostatic charge-discharge measurements at 2.5 mA cm^{-2} using nafion and bipolar membrane.

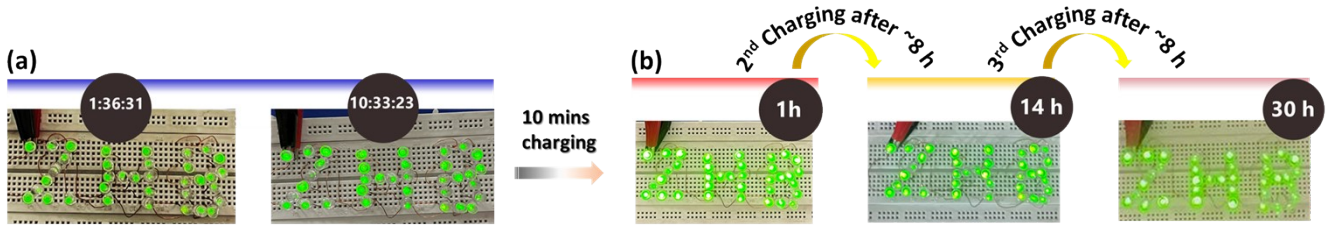

Figure S45. Photographs showing 35 LEDs glowing while connected to the batteries at different times.

References

1. A. Maljusch, T. C. Nagaiah, S. Schwamborn, M. Bron and W. Schuhmann, *Analytical Chemistry*, 2010, **82**, 1890-1896.
2. T. C. Nagaiah, D. Schäfer, W. Schuhmann and N. Dimcheva, *Analytical Chemistry*, 2013, **85**, 7897-7903.
3. A. Joshi, W. Schuhmann and T. C. Nagaiah, *Sensors and Actuators B: Chemical*, 2016, **230**, 544-555.
4. A. Tiwari, V. Singh, D. Mandal and T. C. Nagaiah, *Journal of Materials Chemistry A*, 2017, **5**, 20014-20023.
5. V. Singh, S. D. Adhikary, A. Tiwari, D. Mandal and T. C. Nagaiah, *Chemistry of Materials*, 2017, **29**, 4253-4264.
6. S. D. Adhikary, A. Tiwari, T. C. Nagaiah and D. Mandal, *ACS Applied Materials & Interfaces*, 2018, **10**, 38872-38879.
7. V. Singh and T. C. Nagaiah, *Journal of Materials Chemistry A*, 2019, **7**, 10019-10029.
8. S. Mehta, D. Gupta and T. C. Nagaiah, *ChemElectroChem*, 2022, **9**, e202101336.
9. D. Gupta, S. Chakraborty, R. G. Amorim, R. Ahuja and T. C. Nagaiah, *Journal of Materials Chemistry A*, 2021, **9**, 21291-21301.
10. S. Mehta, S. Kaur, K. Garg, M. Singh and T. C. Nagaiah, *Angewandte Chemie International Edition*, **n/a**, e202505593.
11. S. Kaur, K. Garg and T. C. Nagaiah, *ACS Energy Letters*, 2025, **10**, 1430-1438.
12. S. Mehta, N. Elmerhi, S. Kaur, A. K. Mohammed, T. C. Nagaiah and D. Shetty, *Angewandte Chemie International Edition*, 2025, **64**, e202417403.
13. S. Kaur, K. C. Ranjeesh, K. Garg, S. Gaber, S. Mehta, T. C. Nagaiah and D. Shetty, *Journal of Materials Chemistry A*, 2024, **12**, 8516-8525.
14. L. Li, N. Limani, R. P Antony, S. Dieckhöfer, C. Santana Santos and W. Schuhmann, *Small Science*, 2024, **4**, 2300283.
15. A. Goryachev, M. Etzi Coller Pascuzzi, F. Carlà, T. Weber, H. Over, E. J. M. Hensen and J. P. Hofmann, *Electrochimica Acta*, 2020, **336**, 135713.
16. D. Gupta, A. Kafle, A. Chaturvedi and T. C. J. C. Nagaiah, 2021, **8**, 2858-2866.
17. J. P. Perdew, J. A. Chevary, S. H. Vosko, K. A. Jackson, M. R. Pederson, D. J. Singh and C. Fiolhais, *Physical Review B*, 1992, **46**, 6671-6687.
18. G. Kresse and D. Joubert, *Physical Review B*, 1999, **59**, 1758-1775.
19. M. P. Teter, M. C. Payne and D. C. Allan, *Physical Review B*, 1989, **40**, 12255-12263.
20. S. Grimme, J. Antony, S. Ehrlich and H. Krieg, *The Journal of Chemical Physics*, 2010, **132**.
21. S. Gaber, A. K. Mohammed, B. H. Javaregowda, J. I. Martínez, P. P. Sánchez, F. Gándara, K. Krishnamoorthy and D. Shetty, *Angewandte Chemie International Edition*, 2024, **63**, e202409256.
22. J. K. Nørskov, T. Bligaard, A. Logadottir, J. R. Kitchin, J. G. Chen, S. Pandelov and U. Stimming, *Journal of The Electrochemical Society*, 2005, **152**, J23.
23. L. J. J. Janssen, L. M. C. Starmans, J. G. Visser and E. Barendrecht, *Electrochimica Acta*, 1977, **22**, 1093-1100.
24. K. S. Exner, J. Anton, T. Jacob and H. Over, *Angewandte Chemie International Edition*, 2016, **55**, 7501-7504.
25. T. Lim, J. H. Kim, J. Kim, D. S. Baek, T. J. Shin, H. Y. Jeong, K.-S. Lee, K. S. Exner and S. H. Joo, *ACS Catalysis*, 2021, **11**, 12232-12246.
26. K. S. Exner, *Physical Chemistry Chemical Physics*, 2020, **22**, 22451-22458.